Catalysis Science & Technology

ROYAL SOCIETY OF CHEMISTRY

PAPER

View Article Online
View Journal | View Issue

Cite this: *Catal. Sci. Technol.*, 2025, **15**, 7200

A computational study on the formation mechanism of naphthalenic species under MTO conditions in H-SSZ-13

Annika E. Enss,[a] Philipp N. Plessow *[a] and Felix Studt [ab]

Received 10th July 2025,
Accepted 30th September 2025

DOI: 10.1039/d5cy00837a

rsc.li/catalysis

A mechanistic pathway for the formation of naphthalene species in the MTO reaction network is proposed, starting from polymethylbenzenes, formaldehyde and an olefin as reactants. The mechanism is investigated computationally for di-, tri- and tetramethylbenzene and *n*-butene in the H-SSZ-13 zeolite. The highest free energy barriers at 400 °C are 202, 201 and 236 kJ mol^{-1}, respectively. After the second ring is formed, the free energy profile of the substrate with the highest degree of methylation is clearly the least favorable, due to space restrictions in the CHA cell. The free energy barriers are higher than olefin production barriers from the aromatic cycle, but still in an accessible range under MTO conditions, which makes them relevant as deactivation reactions.

1 Introduction

The methanol-to-olefins[1,2] process is a possible way for the chemical industry to replace crude oil with sustainably produced methanol.[3] Two industrially employed catalysts are H-SAPO-34 (ref. 4) and H-ZSM-5.[5] The process proceeds through a dual-cycle mechanism,[6] in which olefins and aromatics act as co-catalytic species. In the understanding of the catalytic reactivity, computational analysis has proven to be a valuable tool.[7–9]

During the reaction, zeolite catalysts suffer coking after a sufficiently long time on stream. Large polycyclic aromatics are usually referred to as 'coke', but deactivation is caused by any molecule blocking the acid sites and hindering diffusion.[1] Coke formation mechanisms depend on zeolite topology,[10] since the required space to form bicyclic or larger molecules is given in large cavity zeolite structures as chabazite (CHA) or three-dimensional 12-ring structures as zeolite beta (BEA),[11] but not in 10-ring structures like MFI.[12] It could be observed spectroscopically that deactivation on H-ZSM-5 is caused by externally formed coke species, whereas larger coke species formed inside the zeolite crystal are responsible for deactivation of H-SAPO-34 by hindering diffusion through the pores.[13] Co-feeding of water is reportedly able to suppress coking in CHA-structured zeolites.[14,15]

On the pathway to polycyclic molecules, naphthalenes are among the first polyaromatic species to be found,[11,16,17] and grow into larger polyaromatic systems, even connecting molecules in adjacent cages.[18] However, naphthalene species not only form part of deactivating coke, but also can act as active co-catalysts in the aromatic cycle with a higher selectivity for light olefin formation, despite being only one-third as active as methylbenzenes.[17,19] In a theoretical assessment by Hemelsoet *et al.*,[20] methylation barriers for naphthalene species were shown to be in a feasible energy range in H-SAPO-34 and H-SSZ-13, for a number of up to three methyl groups already present in the ring. However, the first reactions of the side-chain cycle with naphthalene as a co-catalyst were reported to have too low intrinsic rate coefficients to be considered for ethylene formation. In a subsequent study, which combined computations and *in situ* UV-vis spectroscopy, fused aromatics with more than two rings were also considered.[21] In general, naphthalene rings are less reactive towards methylation than benzenes, though lower methylated naphthalenes with up to three methyl groups can almost reach the reactivity of hexamethylbenzene. Methylation barriers increase for tetramethylnaphthalenes due to steric constraints, and are even higher for phenantrenes. It is therefore concluded that phenantrenes and highly methylated naphthalenes can be considered as inactive coke species. On the other hand, Wang *et al.* calculated reaction barriers for the side-chain mechanism of polymethylbenzenes and naphthalenes, and their activities were found to be similar in the supercages of H-MCM-22.[22]

Recently, the naphthalene catalyzed cycle has gained more interest, as it could help to extend the catalyst lifetime through different treatments. Zhou *et al.*[23] investigated a steam cracking treatment to transform inactive coke into

[a] *Institute of Catalysis Research and Technology, Karlsruhe Institute of Technology, Hermann-von-Helmholtz-Platz 1, 76344 Eggenstein-Leopoldshafen, Germany. E-mail: philipp.plessow@kit.edu*
[b] *Institute for Chemical Technology and Polymer Chemistry, Karlsruhe Institute of Technology, Engesserstrasse 18, 76131 Karlsruhe, Germany*

active naphthalenic species. This avoids the loss of active hydrocarbon-pool species during coke removal, increasing the carbon efficiency. The experiments resulted in a high light olefin selectivity of 85%. In a different approach, Wang *et al.* tested a precoking and steaming treatment on H-SAPO-34 to build up naphthalene molecules in the zeolite crystal center before the reaction.[24] This leads to an increased light olefin selectivity of 89% and a 3.7-times longer catalyst lifetime than the untreated sample. A further study on the H-SAPO-34 catalyst by the group of Liu[25] showed that co-feeding water could assist the naphthalene-catalyzed side-chain cycle and increase the selectivity for ethylene, while simultaneously reducing coke deposition.

In the literature, several pathways based on both experimental and computational findings are proposed by which naphthalene species (Fig. 1d) could be formed,[11,14,16,22,26–34] and relevant intermediates are presented in Fig. 1. In the following, we will give a short review on the current state of research, and explain how we developed our mechanistic investigation based on those results.

The analysis of coke residues in zeolites after the MTO reaction gives a hint on the possible formation route of naphthalenes. Earlier studies from Bjørgen *et al.* on H-beta,[11] H-MOR and H-MCM-22[26] revealed the presence of dihydrotrimethylnaphthalene (Fig. 1c) as the smallest naphthalene species. Notably, no tetrahydronaphthalenes (Fig. 1b) were detected in these studies. The reaction was conducted with ^{13}C-labeled MeOH, and the ^{13}C content of methylnaphthalene species was in good agreement with the cumulative ^{13}C content of a methylated benzene and an olefinic species.[26] Another more recent study on coke residues in H-SAPO-34 by Luo *et al.* further revealed the presence of methylated 2,3-dihydro-1*H*-indenes (Fig. 1a) as a bridge between benzenes and naphthalenes.[16] In their proposed route to larger polyaromatic molecules, the dihydroindene species appear after alkylated benzenes, formed by dehydrogenation and cyclization of the alkyl side chain.

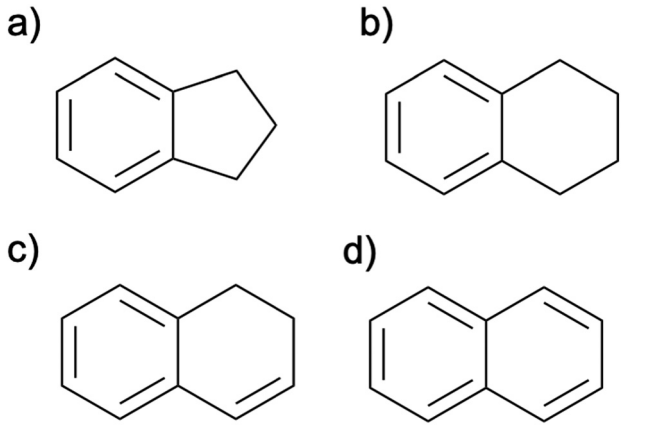

Fig. 1 Relevant structures on the path from polymethylbenzenes to naphthalenes. For simplicity, the unmethylated structures are shown. a) 2,3-dihydro-1*H*-indene b) 1,2,3,4-tetrahydronaphthalene c) 1,2-dihydronaphthalene d) naphthalene.

Another approach to cyclization is the direct formation of an unsaturated sidechain, omitting the dehydrogenation of the alkyl sidechain. In a study on the influence of HCHO in the MTO process,[14] Bollini *et al.* show a possible reaction mechanism involving HCHO. Through the reaction with benzene, benzylcations can be formed, and addition of an olefin leads to an unsaturated sidechain at the benzene ring. If the sidechain contains four or more carbons, cyclization to a naphthalene species is possible. The observed inhibitory effect of water on this deactivation pathway is due to lower formaldehyde concentrations, limiting this deactivation pathway of formaldehyde.[14] The presence of formaldehyde in MTO reactions was previously investigated and found to accelerate the deactivation of the catalyst by increasing aromatics and polyaromatics formation.[27–32] Other experimental studies using photoelectron photoion coincidence spectroscopy found cyclopentadienes, fulvenes and indenes as reaction intermediates in coke formation.[35,36] Possible reaction mechanisms are the Diels–Alder dimerization of cyclopentadiene with subsequent isomerization to a tetrahydronaphthalene species[35] and the reaction of benzene and propyne to an indene species and further ring expansion to naphthalene.[35] Fulvenes are formed in the reaction of cyclopentadienes and formaldehyde, and can isomerize to alkylated benzenes and after further alkylation and cyclization to naphthalenes.[36] The reaction of dienes and formaldehyde to cyclopentadienes was shown to contribute considerably to zeolite deactivation by Foley *et al.*[32]

Naphthalene formation was also investigated computationally. Wang *et al.* calculated reaction barriers with the ωB97X-D functional for the formation of benzene, naphthalene, anthracene and phenantrene in the supercages of the H-MCM-22 zeolite.[22] Their investigated mechanism includes alkylation of benzene, dehydrogenation of the side chain, cyclization to tetrahydronaphthalene and subsequent dehydrogenation to naphthalene. The highest barriers found are the HT steps, with intrinsic free energy barriers between 155 and 165 kJ mol^{-1} at 400 °C.

In a combined experimental and computational study by the group of Fan,[33] alkylation of methylbenzenes with cyclic carbocations was proposed as a pathway to form naphthalenes. This way, the first species are cross-linked polyaromatics. They calculated barriers for several pathways in zeolites H-ZSM-5, H-SSZ-13 and H-beta, and reported the highest intrinsic free energy barriers of naphthalene formation for H-SSZ-13 to be in the range of 111–134 kJ mol^{-1} at 300 °C.

Yu *et al.* investigated the process leading to the formation of coke using GC-MS, thermogravimetry and DFT calculations to analyze the retained species in H-SAPO-34.[34] They identified three coke precursor species, for which reaction barriers of two possible routes to naphthalene were calculated. Their calculations start from an already alkylated aromatic ring, with an unsaturated butene side chain, which can cyclize either directly to a tetrahydronaphthalene, or to a 2,3-dihydro-1*H*-indene species, which expands after the first hydrogen transfer to a trihydronaphthalene cation. In this

pathway, the tetrahydronaphthalene species is not observed. In the study of Yu *et al.*, a 72-T model of H-SAPO-34 and the ωB97X-D functional was used. The pathway *via* the tetrahydronaphthalene species was reported to have lower intrinsic barriers than the pathway involving the dihydroindene species, though both pathways have feasible reaction barrier heights. The naphthalene formation pathway proceeding through 2,3-dihydro-1*H*-indene species is supported by the findings of Luo *et al.*,[16] who found trace amounts of methylated dihydroindene species in the retained material after the MTO reaction on H-SAPO-34.

In this work, we investigate the formation mechanism of naphtalenes in H-SSZ-13 using DFT calculations. As reactants, we consider di-, tri- and tetramethylbenzene along with formaldehyde and *n*-butene as olefins. Based on the computed free energy barriers, we compare the expected rate of deactivation with catalytic activities deduced from previous work.

2 Computational methods

In our computational model, the H-SSZ-13 unit cell contains 36 T-atoms (Si/Al ratio = 35), and its lattice parameters were optimized in earlier work[37] to a = 13.625 Å, b = 13.625 Å and c = 15.067 Å. Geometry optimizations were done with DFT calculations using the dispersion-corrected PBE- D3[38,39] functional. A convergence criterion of 0.001 eV Å^{-1} and an energy-cutoff of 400 eV were used. Calculations were carried out with the Vienna Ab initio Simulation Package (VASP) version 6.4.3 in the Atomic Simulation Environment[40] (ASE) with the projector-augmented wave method[41,42] and k-point sampling only at the Γ-point. Transition states were calculated with the automated relaxed potential energy surface scans (ARPESS) method.[43] Vibrational frequencies were calculated using the harmonic oscillator, rigid rotator and free translator approximations. Since low harmonic frequencies lead to large errors in free energy calculations, we raised the vibrations below 12 cm^{-1} to this value.[44,45] For transition states, vibrational analysis confirmed the presence of a single imaginary frequency, and subsequent distortion along the direction of the imaginary frequency was performed to confirm the connectivity of reactant and product states. Calculations with PBE-D3 severely underestimate activation energies.[46–48] We therefore computed periodic single-point energies with the dispersion-corrected ωB97M-D4 functional,[49–51] which was shown to describe barriers much more accurately than the PBE-D3 functional and mean absolute errors were within 10 kJ mol^{-1} deviation of CCSD(T) cluster calculations.[47]

3 Results and discussion

Zeotypes in the chabazite (CHA) framework are routinely studied as catalysts for the MTO process, mainly H-SAPO-34, and also H-SSZ-13.[1,2,4,52,53] From a computational point of view, the CHA framework is attractive because of its simplicity, as it has only one unique T-site and a relatively small unit cell. In this work, we chose to study H-SSZ-13, because this allows us to compare directly with our previous computational investigations on this catalyst. We note that it is furthermore relatively easy to transfer calculations from H-SSZ-13 to H-SAPO-34.[54–56]

We have investigated a mechanistic pathway for naphthalene formation that involves polymethylbenzenes (polyMB), HCHO and olefins as reactants based on several proposals in the literature, in particular the work of Bollini *et al.*[14] Benzyl carbenium ions and dihydroindenes are crucial intermediates, which is supported by the work of Yu *et al.*[34] and the pathway does not include tetrahydronaphthalene species, in alignment with findings from Bjørgen *et al.*[11,26]

Fig. 2a) shows the reaction mechanism we investigated. First, HCHO couples with the aromatic ring to benzyl alcohol (**2**), and releases H_2O to form the benzyl cation (**4**). This has various mesomeric structures, in which the charge is distributed across the ring, and is therefore relatively stable. *n*-Butene is added from the gas phase, and the cation is alkylated at the methylene group. Structure **5**, a dihydroindene cation, is either formed in one step (in the case of tetraMB as the substrate), or *via* a four-membered ring intermediate (**4′**). Deprotonation of structure **5** leads to a dihydroindene species (**6**). To reach the naphthalene product, the dihydroindene intermediate must release two units of H_2 and expand the 5-membered ring to a 6-membered ring. The release of H_2 units is modeled in two steps: first, a hydrogen transfer (HT) step where a hydride is abstracted from the neutral molecule by a surface methoxy species (SMS), followed by the deprotonation of the cation to recover the acid site, similar to the work of Wang *et al.*[22] The first HT occurs at the ethyl side chain at the indene 5-membered ring, subsequently the cationic side chain (**7**) inserts into the ring to expand to a 6-membered ring structure, the trihydronaphthalene ion (**8**). These are two separate steps for the highest methylated sample, but di- and trimethylbenzene ring expansion occurs spontaneously after abstracting hydrogen, passing through intermediate **7**, which is not a stable intermediate in these two cases. After deprotonation to a dihydronaphthalene species (**9**), the second HT and deprotonation lead finally to the naphthalene product. The oxidative HT step could in principle be also modeled as the reaction with the acidic proton of the Brønsted acid site, resulting in H_2 formation. We decided to use CH_4 formation from a surface methoxy species (SMS) as the model reaction, because it shows lower reaction barriers than formation of H_2 by 15–20 kJ mol^{-1} (see Fig. S1), in addition to a more favorable reaction free energy at the investigated temperature. In previous computational work, this reaction was also used to model HT reaction steps.[22] Knowing that polyMBs are part of the aromatic cycle, we chose to start from these structures rather than benzene or butylbenzene. They are present in relevant concentrations, and are more stable in the cages than pure benzene.[57] Following the proposal of Bollini *et al.*,[14] we chose the addition of HCHO to the polyMB to introduce an unsaturated side-chain, since removing hydrogen from a methyl group has very high barriers and HCHO was already shown to play a role in the formation of deactivating species.[29,32] As the reacting olefin, we chose *n*-butene, which will lead to a

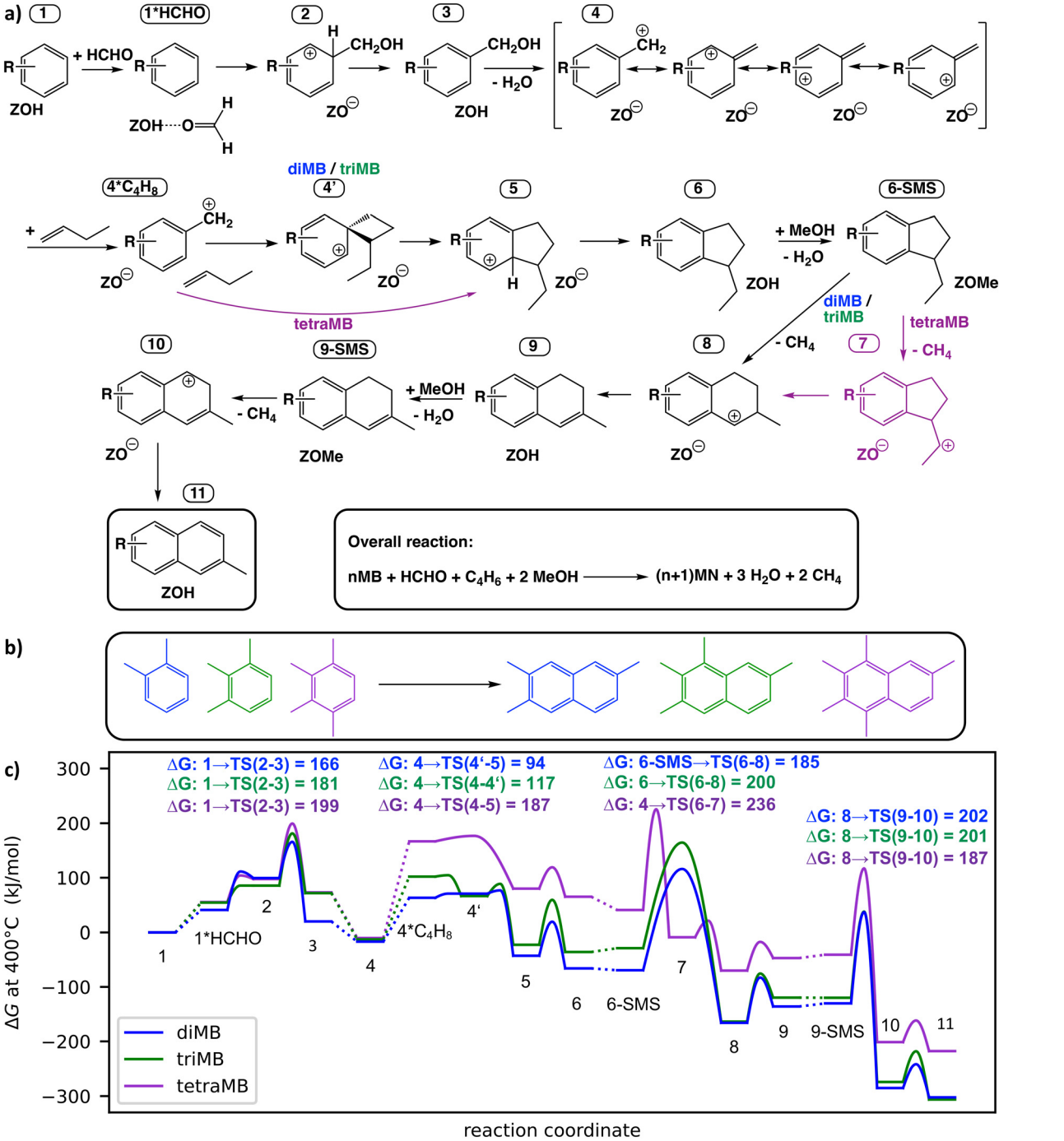

Fig. 2 a) Reaction scheme of the investigated naphthalene formation mechanism. –R = dimethyl, trimethyl, tetramethyl. *n*MB = *n*-methylbenzene, (*n* + 1). MN = (*n* + 1)-methylnaphthalene. b) Investigated isomers of reactants and products. c) Gibbs free energy diagrams of reaction free energies for naphthalene formation with di-, tri- and tetramethylbenzene. Reaction barrier heights are indicated above the respective barriers. Reaction temperature is 400 °C; reference pressure = 1 bar.

secondary cation in the first hydride transfer reaction (state 7, see below). A reaction with propene or isobutene would lead to a primary cation in the first HT step. The corresponding reaction barriers for the reaction of propene or isobutene with diMB are slightly higher (5–10 kJ mol^{-1}) than that for the reaction with *n*-butene (see Fig. S2). When we investigated the addition of butene to the benzyl carbenium ions, we did not observe the formation of a cationic side chain, but rather the concerted addition of the olefin's double bond to the methylene group and benzene ring, yielding a bicyclic species, in accordance with the findings from Yu *et al.*[34] Additionally, our mechanism does not give tetrahydronaphthelene species but directly the dihydronaphthalene species, like in the study of Bjørgen *et al.*[12]

In Fig. 2c), the free energy pathways at 400 °C are shown for the three investigated methylbenzenes (di-, tri- and tetramethylbenzene). Barrier heights are indicated in the figure, and are taken as difference between the free energy of the transition state and the free energy of the most stable preceding intermediate state. This state is explicitly named in the figure for each barrier. Our model catalyst H-SSZ-13 has a CHA structure, with cages large enough to accommodate bicyclic aromatic molecules, connected by 8-ring windows which hinder the diffusion of larger branched olefins or benzenes.[58] We therefore consider methylbenzenes in the following as trapped species, while other reactants (HCHO, MeOH, *n*-butene) are able to diffuse through the zeolite pores. This justifies us to take the adsorbed methylbenzene as the reference in Fig. 2c) and all other reactants in the gas phase. The corresponding isomers of polyMBs are depicted in Fig. 2b).

After overcoming the first barriers, the benzylcation is the first intermediate structure more stable than the inital state at −17, −13 and −10 kJ mol^{-1} for di-, tri-, and tetramethylbenzene, respectively. The subsequent co-adsorption of *n*-butene leads to an increase in free energy, with an alkylation barrier that is lower than the preceding alcohol formation barrier in all three cases. The large differences between the three samples is explained by the different co-adsorption free energies, since the internal barriers from the co-adsorbed state are more similar (6, 2.5 and 10 kJ mol^{-1}) than the total barriers (94, 117 and 198 kJ mol^{-1}).

SMS formation barriers in the presence of polymethylbenzenes were calculated previously in our group and found to be mostly in the feasible range of 140–160 kJ mol^{-1},[57] so that we omitted them in the present study.

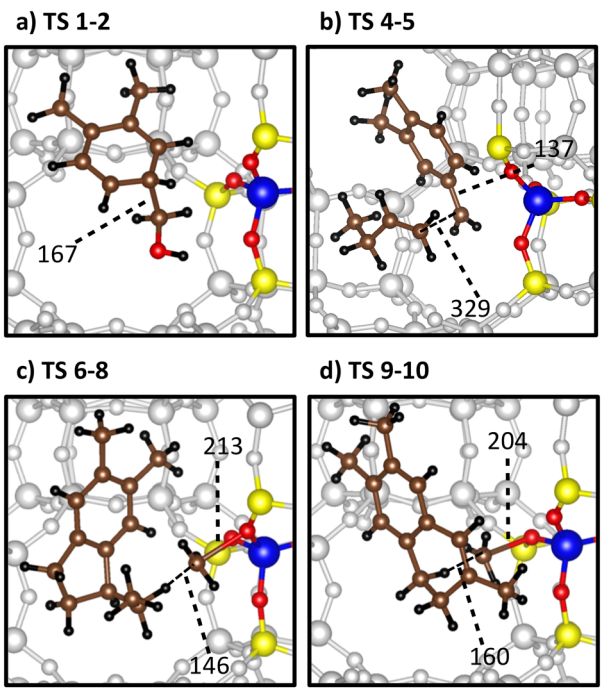

Fig. 3 Structures of important transition states in the naphthalene formation process starting from dimethylbenzene. Color code: blue: Al, yellow: Si, red: O, brown: C, black: H. Bond lengths indicated in pm.

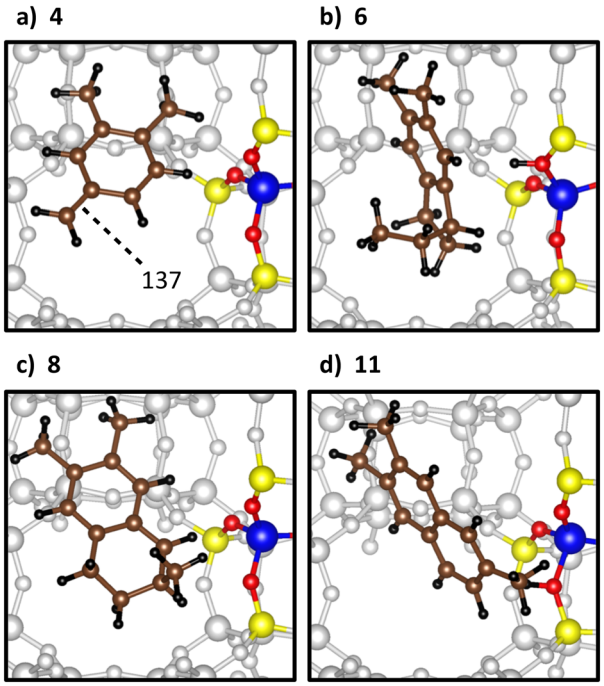

Fig. 4 Structures of important intermediates in the naphthalene formation process starting from dimethylbenzene. Color code: blue: Al, yellow: Si, red: O, brown: C, black: H. Bond lengths indicated in pm.

While the formation of the benzylcation is energetically similar for different methylsubstitutions, starting from the cyclization to the second fused ring, the tetramethylethyldihydroindene and later the penta-methylnaphthalene species are higher in free energy than the respective indermediates and products with fewer methyl groups. To investigate framework effects on these energetics, we compared the species **1**, **6**, **9** and **11** for each methylation pattern in the gas phase with their counterparts inside the zeolite. The differences show clearly that the energetic penalty on the highest methylated species is due to confinement effects, not general stability (see Fig. S3). This is in line with findings from Haw and Marcus, who did not observe naphthalene species with more than four methyl groups in H-SAPO-34.[59]

Fig. 3 and 4 show the important transition states and intermediate structures of the reaction pathway, exemplary for dimethylbenzene. The first transition state (Fig. 3a) shows the coupling of diMB with the protonated formaldehyde cation. The newly formed C–C bond is already present in the TS structure, with a bond length of 167 pm. The stable benzylcation (**4**) formed after the dehydrogenation of the benzylalcohol is shown in Fig. 4a). The depicted bond length of the methylene group (137 pm) indicates that bond is rather a double bond than a single bond, meaning that the positive charge is rather located at the aromatic ring than at the CH_2-unit, as represented by the mesomeric structures in Fig. 2a). The transition state of the alkylation (Fig. 3b) shows that the distance between the carbon atoms forming a bond is rather large in the TS (329 pm). During bond formation, the distance between the methylene group and

the ring-carbon enlarges to the typical bond distance of a single bond. The dihydroindene species is shown in Fig. 4b). The following image (Fig. 3c)) shows the transition state of the first HT step. The hydrogen, methyl group and acid site oxygen form a linear arrangement, and after the removal of methane, the structure relaxes directly to the dihydronaphthalene species (Fig. 4c)) by insertion of the ethyl group into the 5-ring. The second HT step proceeds with a hydrogen from the carbon atom adjacent to the first aromatic ring (Fig. 3d)) and an analogous linear arrangement of reactants, and the following deprotonation of the hydronaphthalene species finally releases the product trimethylnaphthalene (Fig. 4d)).

In the presented mechanism, we assumed the presence of formaldehyde in the reaction mixture. Because it is a highly reactive intermediate, formaldehyde is only observed in trace amounts during the reaction of H-SAPO-34[62] or H-ZSM-5,[29] due to its rapid reaction with olefins or aromatics. ^{13}C-labelling experiments show, however, that formaldehyde enables a fast reaction step, namely the Prins reaction with olefins to dienes, on the formation pathway to aromatics and finally coke.[29] Since HCHO is a small molecule, we assume that diffusion inside the zeolite pore is unhindered. Several mechanisms exist, through which HCHO can be formed in zeolites, such as disproportionation of MeOH into CH_4, HCHO and H_2O,[60,63,64] decomposition of MeOH into HCHO and H_2[61,65,66] or MeOH-mediated hydrogen transfer (HT) to olefins yielding alkanes and HCHO[61,67] (summarized in Fig. 5). In our group, reaction barriers for all of these possible reactions were calculated for Brønsted and Lewis acid sites (LAS) in H-SSZ-13, and found to be in the range of 177–239 kJ mol^{-1} at 400 °C. The lowest free energy barrier was found for the reaction of MeOH and isobutene on LAS (177 kJ mol^{-1}), whereas the highest free energy barrier corresponds to MeOH decomposition on the bulk Brønsted sites (239 kJ mol^{-1}).[61] For hydrogen transfer from MeOH to SMS, leading to CH_4 formation, we found a free energy barrier of 222 kJ mol^{-1} at 748 K in H-ZSM-5,[60] in good agreement with a value of 210 kJ mol^{-1} deduced from experimental kinetics. While the discussion above refers to apparent free energy barriers for formaldehyde formation, we note that apparent activation energies for

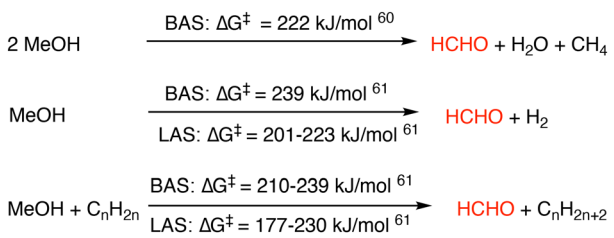

Fig. 5 Possible reactions for HCHO formation on BASs and LASs previously investigated by our group. The indicated reaction barriers were computed at a temperature of 400 °C and a reference pressure of 1 bar for all reactants. Barriers of the first reaction are taken from ref. 60, and for the second and third reactions from ref. 61.

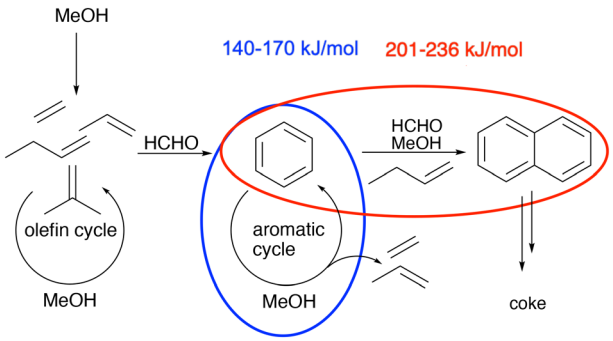

Fig. 6 Placing the results of this work (highlighted in red) in the context of MTO reactions. Reaction barriers for ethylene and propylene formation (highlighted in blue) are taken from ref. 69 and ref. 70.

this reaction are generally lower, for example 75–80 kJ mol^{-1} reported based on experiments in H-ZSM-5 at 621–743 K.[36] For the quoted examples above, with an apparent free activation energy of 222 kJ mol^{-1}, the computed apparent activation energy was 111 kJ mol^{-1}. Since the three reactions shown in Fig. 5 give different reaction free energies, which also strongly depend on partial pressures of the involved gas phase species, we did not include the HCHO formation in the Gibbs free energy diagram Fig. 2b). Overall, the formation of HCHO has one of the highest free energy barriers in the process, followed by HT reactions, thus stressing again the critical importance of formaldehyde in deactivation processes.

To assess the relevance of the presented naphthalene formation mechanism, we compare our results with other MTO reactions involving benzenes, shown in Fig. 6. The methylation of benzenes proceeds easily,[57,68] and the reported barriers in the side-chain (168 kJ mol^{-1} in H-SSZ-13[69]) and paring mechanism (142 k mol^{-1} in H-SSZ-13,[70] 139 kJ mol^{-1} in H-SAPO-34[56] and 168 kJ mol^{-1} in H-ZSM-5[56]) with hexamethylbenzene are in general lower than the naphthalene formation barriers found in this work. Free energy barriers for ethene and propene production computed previously[69,70] are thus 30–60 kJ mol^{-1} lower than those for naphthalene formation, which we therefore expect to have reaction rates that are 3 to 6 orders of magnitude lower. Bleken *et al.* found that at 400 °C, H-SSZ-13 converted roughly 280 MeOH molecules per active site before deactivation[53] (see the SI for details), which agrees with a difference of 3 orders of magnitude between rates for olefin synthesis and deactivation. We note that the comparison of different processes in terms of free energy barriers is of course simplified. While the free energies contain the information for reaction rate constants, a full kinetic simulation will also depend on coverages and diffusion. We note in passing that activation energies (rather than activation free energies) are in general insufficient to predict reaction rates and catalytic activities since they lack the activation entropy that will enter the calculation of a reaction rate constant with transition state theory (TST) either as a prefactor or – equivalently – as a contribution to the activation free energy.

Conclusion and outlook

In summary, we provide a computational analysis of a naphthalene formation mechanism involving polymethylbenzenes, formaldehyde, and butene. The process is downhill in free energy, with reaction barriers of up to 202 kJ mol^{-1} (diMB), 201 kJ mol^{-1} (triMB), and 236 kJ mol^{-1} (tetraMB), which clearly shows a preference of naphthalene being produced from lower methylated benzenes. In this case, the number of methyl groups in the reactant has the opposite effect than in olefin formation processes, where the highest methylated benzenes show the highest reactivity in H-SAPO-34.[55,68,71] Thus, an increased presence of highly methylated benzenes in the CHA cages might slow down the process of coking. The reaction barriers of naphthalene formation found here are in an energy range accessible at relevant temperatures, but still higher than barriers for olefin formation, so that coke formation does not occur immediately. The reactive formaldehyde has a dual role in both forming reactive aromatics and unreactive coke species.[14,27,32,36,61,67]

We expect that the presented pathway is also viable in the industrially relevant H-SAPO-34 catalyst because of the analogous CHA structure, and the transferability of reaction mechanisms between H-SSZ-13 and H-SAPO-34 has been shown previously for both olefin and aromatic cycles.[54,56] Further studies on this mechanism can include a different choice of the reacting olefin (for example propene or isobutene instead of *n*-butene). In H-ZSM-5, steric restrictions inside the channels and intersections are more severe,[12] so that even highly methylated benzenes can be considered as deactivating coke species and the olefin cycle is acting dominantly over the aromatic cycle.[72] Larger graphitic coke species are thus rather formed at pore openings on the external catalyst surfaces.[13] Inside the zeolite pores, coke formation begins with polymethylated benzenes in the channel intersections, forming polyaromatics up to tricyclic species, which could be observed in the straight channels.[73,74] Qi *et al.* observed that with a naphthalene co-feed, methanol conversion at low temperatures (250 °C) can be increased over H-ZSM-5, since the naphthalene molecules also show a reactivity in the aromatic cycle, though formation of naphthalene from a pure methanol feed was not observed in their study.[75] This leaves room for further investigations regarding naphthalene formation in H-ZSM-5.

Author contributions

A. E. E. conceptualization, investigation, formal analysis, visualization, writing – original draft, and writing – review and editing; P. N. P. conceptualization, supervision, and writing – review and editing; F. S. conceptualization, supervision, and writing – review and editing.

Conflicts of interest

There are no conflicts to declare.

Data availability

Supplementary information: additional computational information and the total energies in PDF. Structure files in POSCAR format are attached in the ZIP file. See DOI: **https://doi.org/10.1039/D5CY00837A**.

The data presented in the main text (Gibbs free energies) as well as the raw data (total energies and Gibbs free energy contributions) and additional data needed to reproduce this study (Cartesian coordinates of stationary points and harmonic frequencies) is provided as supplementary information (SI).

Acknowledgements

The authors acknowledge support by the state of Baden-Württemberg through bwHPC and the German Research Foundation (DFG) through grant no INST 40/575-1 FUGG (JUSTUS 2 cluster) and bwunicluster. Financial support from the Helmholtz Association, Germany, is also gratefully acknowledged. Gefördert durch die Deutsche Forschungsgemeinschaft (DFG) Projektnummer 434253773.

References

1 U. Olsbye, S. Svelle, M. Bjørgen, P. Beato, T. V. W. Janssens, F. Joensen, S. Bordiga and K. P. Lillerud, *Angew. Chem., Int. Ed.*, 2012, **51**, 5810–5831.
2 U. Olsbye, S. Svelle, K. P. Lillerud, Z. H. Wei, Y. Y. Chen, J. F. Li, J. G. Wang and W. B. Fan, *Chem. Soc. Rev.*, 2015, **44**, 7155–7176.
3 B. J. M. Etzold, M. Hungsberg, M. Ebrahim-Moghaddam, F. Herold, N. Dahmen and F. Studt, *Chem. Eng. Technol.*, 2025, **48**, e70034.
4 D. Chen, K. Moljord and A. Holmen, *Microporous Mesoporous Mater.*, 2012, **164**, 239–250.
5 X. Sun, S. Mueller, H. Shi, G. L. Haller, M. Sanchez-Sanchez, A. C. Van Veen and J. A. Lercher, *J. Catal.*, 2014, **314**, 21–31.
6 S. Ilias and A. Bhan, *ACS Catal.*, 2013, **3**, 18–31.
7 G. Li and E. A. Pidko, *ChemCatChem*, 2019, **11**, 134–156.
8 C. Chizallet, *Top. Catal.*, 2022, **65**, 69–81.
9 C. Chizallet, C. Bouchy, K. Larmier and G. Pirngruber, *Chem. Rev.*, 2023, **123**, 6107–6196.
10 M. Guisnet and P. Magnoux, *Appl. Catal., A*, 2001, **212**, 83–96.
11 M. Bjørgen, *J. Catal.*, 2003, **215**, 30–44.
12 M. Bjørgen, S. Svelle, F. Joensen, J. Nerlov, S. Kolboe, F. Bonino, L. Palumbo, S. Bordiga and U. Olsbye, *J. Catal.*, 2007, **249**, 195–207.
13 D. Mores, E. Stavitski, M. Kox, J. Kornatowski, U. Olsbye and B. Weckhuysen, *Chem. – Eur. J.*, 2008, **14**, 11320–11327.
14 P. Bollini, T. T. Chen, M. Neurock and A. Bhan, *Catal. Sci. Technol.*, 2019, **9**, 4374–4383.
15 M. Luo, Y. Fu, B. Hu, D. Wang, B. Wang and G. Mao, *Appl. Catal., A*, 2019, **570**, 209–217.
16 M. Luo, B. Hu, G. Mao and B. Wang, *ACS Omega*, 2022, **7**, 3277–3283.

17 H. Fu, W. Song and J. F. Haw, *Catal. Lett.*, 2001, **76**, 89–94.
18 N. Wang, Y. Zhi, Y. Wei, W. Zhang, Z. Liu, J. Huang, T. Sun, S. Xu, S. Lin, Y. He, A. Zheng and Z. Liu, *Nat. Commun.*, 2020, **11**, 1079.
19 W. Song, H. Fu and J. F. Haw, *J. Phys. Chem. B*, 2001, **105**, 12839–12843.
20 K. Hemelsoet, A. Nollet, V. VanSpeybroeck and M. Waroquier, *Chem. – Eur. J.*, 2011, **17**, 9083–9093.
21 V. VanSpeybroeck, K. Hemelsoet, K. DeWispelaere, Q. Qian, J. VanderMynsbrugge, B. DeSterck, B. M. Weckhuysen and M. Waroquier, *ChemCatChem*, 2013, **5**, 173–184.
22 S. Wang, Y. Chen, Z. Wei, Z. Qin, T. Liang, M. Dong, J. Li, W. Fan and J. Wang, *J. Phys. Chem. C*, 2016, **120**, 27964–27979.
23 J. Zhou, M. Gao, J. Zhang, W. Liu, T. Zhang, H. Li, Z. Xu, M. Ye and Z. Liu, *Nat. Commun.*, 2021, **12**, 17.
24 C. Wang, L. Yang, M. Gao, X. Shao, W. Dai, G. Wu, N. Guan, Z. Xu, M. Ye and L. Li, *J. Am. Chem. Soc.*, 2022, **144**, 21408–21416.
25 C. Zhang, X. Wu, Y. Zhang, W. Zhang, S. Lin, C. Lou, S. Xu, D. He, L. Wang, Y. Wei and Z. Liu, *Chem Catal.*, 2024, **4**, 101025.
26 M. Bjørgen, S. Akyalcin, U. Olsbye, S. Benard, S. Kolboe and S. Svelle, *J. Catal.*, 2010, **275**, 170–180.
27 A. Hwang, M. Kumar, J. D. Rimer and A. Bhan, *J. Catal.*, 2017, **346**, 154–160.
28 J. S. Martinez-Espin, M. Mortén, T. V. W. Janssens, S. Svelle, P. Beato and U. Olsbye, *Catal. Sci. Technol.*, 2017, **7**, 2700–2716.
29 Y. Liu, F. M. Kirchberger, S. Müller, M. Eder, M. Tonigold, M. Sanchez-Sanchez and J. A. Lercher, *Nat. Commun.*, 2019, **10**, 1462.
30 A. Hwang and A. Bhan, *Acc. Chem. Res.*, 2019, **52**, 2647–2656.
31 B. L. Foley and A. Bhan, *ACS Catal.*, 2020, **10**, 10436–10448.
32 B. L. Foley, B. A. Johnson and A. Bhan, *ACS Catal.*, 2021, **11**, 3628–3637.
33 S. Fan, H. Wang, P. Wang, W. Jiao, S. Wang, Z. Qin, M. Dong, J. Wang and W. Fan, *Chem Catal.*, 2024, **4**, 100927.
34 B. Yu, W. Zhang, Y. Wei, X. Wu, T. Sun, B. Fan, S. Xu and Z. Liu, *Chem. Commun.*, 2020, **56**, 8063–8066.
35 A. Cesarini, S. Mitchell, G. Zichittella, M. Agrachev, S. P. Schmid, G. Jeschke, Z. Pan, A. Bodi, P. Hemberger and J. Pérez-Ramírez, *Nat. Catal.*, 2022, **5**, 605–614.
36 V. Paunović, X. Wu, L. Maggiulli, D. Ferri, P. Hemberger, A. Bodi and J. A. Van Bokhoven, *Catal. Sci. Technol.*, 2024, **14**, 1216–1228.
37 P. N. Plessow and F. Studt, *ACS Catal.*, 2017, **7**, 7987–7994.
38 J. P. Perdew, K. Burke and M. Ernzerhof, *Phys. Rev. Lett.*, 1996, **77**, 3865–3868.
39 S. Grimme, J. Antony, S. Ehrlich and H. Krieg, *J. Chem. Phys.*, 2010, **132**, 154104.
40 A. Hjorth Larsen, J. Jørgen Mortensen, J. Blomqvist, I. E. Castelli, R. Christensen, M. Dułak, J. Friis, M. N. Groves, B. Hammer, C. Hargus, E. D. Hermes, P. C. Jennings, P. Bjerre Jensen, J. Kermode, J. R. Kitchin, E. Leonhard Kolsbjerg, J. Kubal, K. Kaasbjerg, S. Lysgaard, J. Bergmann Maronsson, T. Maxson, T. Olsen, L. Pastewka, A. Peterson, C. Rostgaard, J. Schiøtz, O. Schütt, M. Strange, K. S. Thygesen, T. Vegge, L. Vilhelmsen, M. Walter, Z. Zeng and K. W. Jacobsen, *J. Phys.: Condens. Matter*, 2017, **29**, 273002.
41 G. Kresse and J. Furthmüller, *Phys. Rev. B: Condens. Matter Mater. Phys.*, 1996, **54**, 11169–11186.
42 G. Kresse and D. Joubert, *Phys. Rev. B: Condens. Matter Mater. Phys.*, 1999, **59**, 1758–1775.
43 P. N. Plessow, *J. Chem. Theory Comput.*, 2018, **14**, 981–990.
44 R. Y. Brogaard, R. Henry, Y. Schuurman, A. J. Medford, P. G. Moses, P. Beato, S. Svelle, J. K. Nørskov and U. Olsbye, *J. Catal.*, 2014, **314**, 159–169.
45 R. Y. Brogaard, C.-M. Wang and F. Studt, *ACS Catal.*, 2014, **4**, 4504–4509.
46 T. J. Goncalves, P. N. Plessow and F. Studt, *ChemCatChem*, 2019, **11**, 4368–4376.
47 P. Huber and P. N. Plessow, *ChemPhysChem*, 2025, e2500147.
48 P. N. Plessow, *J. Chem. Theory Comput.*, 2025, **21**, 8518–8532.
49 N. Mardirossian and M. Head-Gordon, *J. Chem. Phys.*, 2016, **144**, 214110.
50 A. Najibi and L. Goerigk, *J. Chem. Theory Comput.*, 2018, **14**, 5725–5738.
51 A. Najibi and L. Goerigk, *J. Comput. Chem.*, 2020, **41**, 2562–2572.
52 E. Borodina, F. Meirer, I. Lezcano-González, M. Mokhtar, A. M. Asiri, S. A. Al-Thabaiti, S. N. Basahel, J. Ruiz-Martinez and B. M. Weckhuysen, *ACS Catal.*, 2015, **5**, 992–1003.
53 F. Bleken, M. Bjørgen, L. Palumbo, S. Bordiga, S. Svelle, K.-P. Lillerud and U. Olsbye, *Top. Catal.*, 2009, **52**, 218–228.
54 C.-M. Wang, Y.-D. Wang, Y.-J. Du, G. Yang and Z.-K. Xie, *Catal. Sci. Technol.*, 2015, **5**, 4354–4364.
55 J. Ke, W.-D. Hu, Y.-J. Du, Y.-D. Wang, C.-M. Wang and Z.-K. Xie, *ACS Catal.*, 2023, **13**, 8642–8661.
56 A. E. Enss, P. N. Plessow and F. Studt, *J. Catal.*, 2024, **432**, 115363.
57 M. Fečík, P. N. Plessow and F. Studt, *ACS Catal.*, 2020, **10**, 8916–8925.
58 A. T. Smith, P. N. Plessow and F. Studt, *Chem. Phys.*, 2021, **541**, 111033.
59 J. F. Haw and D. M. Marcus, *Top. Catal.*, 2005, **34**, 41–48.
60 F. M. Kirchberger, Y. Liu, P. N. Plessow, M. Tonigold, F. Studt, M. Sanchez-Sanchez and J. A. Lercher, *Proc. Natl. Acad. Sci. U. S. A.*, 2022, **119**, e2103840119.
61 A. E. Enss, P. Huber, P. N. Plessow and F. Studt, *J. Phys. Chem. C*, 2024, **128**, 15367–15379.
62 Z. Wei, Y.-Y. Chen, J. Li, P. Wang, B. Jing, Y. He, M. Dong, H. Jiao, Z. Qin, J. Wang and W. Fan, *Catal. Sci. Technol.*, 2016, **6**, 5526–5533.
63 G. J. Hutchings, L. J. Van Rensburg, W. Pickl and R. Hunter, *J. Chem. Soc., Faraday Trans. 1*, 1988, **84**, 1311.
64 Z. Wei, Y.-Y. Chen, J. Li, W. Guo, S. Wang, M. Dong, Z. Qin, J. Wang, H. Jiao and W. Fan, *J. Phys. Chem. C*, 2016, **120**, 6075–6087.
65 Y. Liu, S. Müller, D. Berger, J. Jelic, K. Reuter, M. Tonigold, M. Sanchez-Sanchez and J. A. Lercher, *Angew. Chem., Int. Ed.*, 2016, **55**, 5723–5726.

66 V. Paunović, P. Hemberger, A. Bodi, R. Hauert and J. A. Van Bokhoven, *ACS Catal.*, 2022, **12**, 13426–13434.
67 S. Müller, Y. Liu, F. M. Kirchberger, M. Tonigold, M. Sanchez-Sanchez and J. A. Lercher, *J. Am. Chem. Soc.*, 2016, **138**, 15994–16003.
68 B. Arstad, J. B. Nicholas and J. F. Haw, *J. Am. Chem. Soc.*, 2004, **126**, 2991–3001.
69 P. N. Plessow and F. Studt, *ACS Catal.*, 2023, **13**, 624–632.
70 P. N. Plessow, A. E. Enss, P. Huber and F. Studt, *Catal. Sci. Technol.*, 2022, **12**, 3516–3523.
71 B. Arstad and S. Kolboe, *J. Am. Chem. Soc.*, 2001, **123**, 8137–8138.
72 C. Liu, E. A. Uslamin, E. A. Pidko and F. Kapteijn, *ACS Catal.*, 2023, **13**, 5205–5212.
73 J. T. C. Wennmacher, S. Mahmoudi, P. Rzepka, S. Sik Lee, T. Gruene, V. Paunović and J. A. Van Bokhoven, *Angew. Chem.*, 2022, **134**, e202205413.
74 P. Rzepka, D. Sheptyakov, C. Wang, J. A. Van Bokhoven and V. Paunović, *ACS Catal.*, 2024, **14**, 5593–5604.
75 L. Qi, J. Li, Y. Wei, L. Xu and Z. Liu, *Catal. Sci. Technol.*, 2016, **6**, 3737–3744.